Final Technical Report

Submitted to the U.S. Geological Survey

USGS Award Number: G23AP00287

Title of Award: Kinematic and Paleoseismic Investigation of an Upper-Plate Fault on Chirikof Island: A Potential Tsunami-Seismic Hazard Source within the Alaska Subduction Zone

Principal Investigators: Kristin Morell and Suoya Fan

Affiliations: Department of Earth Science, University of California, Santa Barbara

Address: 1006 Webb Hall, University of California, Santa Barbara, CA 93106

Contact Information:

Kristin Morell: kmorell@ucsb.edu, 805-825-5231

Suoya Fan: suoyafan@ucsb.edu, 713-504-1902

Award Term: Jun 1, 2023 – May 31, 2024

Abstract

Along the Alaska subduction zone, the section between the Shumagin Islands and Semidi Islands exhibits an along-strike transition from relatively weak interface coupling in the west to strong coupling in the east. In this transition zone, megathrust ruptures during two recent large earthquakes in 2020 and 2021 partially filled the previously identified Shumagin seismic gap, implying a potential increased probability of megathrust rupture in the strongly coupled section to the east. Here, we present new field observations that argue for a Quatenary-active upper crustal fault cutting across Chirikof Island, a remote 116 km^2 island that lies within this transition in megathrust coupling. We investigated the geometry, surface displacement, and seismic activity of the Chirikof Fault in the southwestern part of the island by conducting tectonic geomorphologic surveys augmented by offshore bathymetry mapping. We find that the Chirikof Fault is a ~60-degree arcward-dipping normal fault that has hosted one or more surface-rupturing earthquakes that have resulted in ~4.0 m to ~9.5 m of vertical separation across a regionally extensive surface of glacial till, which may date to the last glacial maximum. This Chirikof normal fault may be related to the previously-recognized large-scale normal-sense splay fault that has been recognized on deep seismic profiles 320 km along strike to the southeast. Bathymetry data and offshore legacy seismic profiles to the northeast of Chirikof island show that presumed late Pliocene strata have been gently folded and unconformably overlain by intact younger sediments, with no significant recent displacement observed across the Chirikof Fault. These observations suggest that the active Chirikof Fault may tip out several kilometers offshore of Chirikof Island to the northeast. Further to the northeast, 250 km along strike in the Kodiak Islands segment, our recent thermochronology analyses and thermal history modeling reveal persistent thrusting along an active splay fault, Kodiak Shelf Fault, over the past 6-7 Ma. Therefore, we suggest that the Chirikof Island area may represent an NE to SW along-strike transition from active forearc internal shortening to extension.

1. Introduction

The Shumagin, Semidi, and Kodiak Island segments (Fig. 1) exhibit the most significant along-strike variations in accretionary wedge structure, morphology, and seismicity along the entire Alaska subduction zone (e.g. Shillington et al., 2015; Lynner, 2021). A better understanding of the structures within and across these segments is therefore critical to assess a series of outstanding questions about the conditions and dynamics of the Alaskan accretionary wedge, including how structures correlate along-strike, where mechanical heterogeneities are located within the wedge, what mechanisms are responsible for wedge growth, and how elastic-inelastic strain is partitioned across seismic cycles. In the Shumagin and Kodiak Island segments, forearc splay fault systems have been recognized and may be tsunamigenic (Bécel et al., 2017; Ramos et al., 2022). However, the forearc geology in the Semidi segment between them remains poorly understood due to a lack of accessible onshore records and a paucity of high-resolution geophysical data. The Chirikof Island within the Semidi segment and the Chirikof Fault, an onshore fault that cuts through Chirikof Island, provide an exceptional opportunity to investigate the tectonics and forearc upper-plate fault activity in the Semidi segment.

Chirikof Island lies above a key section of the megathrust that exhibits a complex overlapping pattern of past large megathrust rupture and lateral gradients in megathrust behavior.

Chirikof Island is positioned above the eastern edge of the recent 29 July 2021 MW 8.2 Chignik earthquake, an event that was triggered by stress changes caused by the first 2020 MW 7.8 thrust earthquake (Elliott et al., 2022) and also overlaps in rupture area with the great 1938 MW 8.2 earthquake (e.g. Boyd and Lerner-Lam, 1988; Johnson and Satake, 1994; Freymueller et al., 2021; Liu et al., 2022). The combined rupture area of the 2020 and 2021 thrust events coincides with an along-strike transition in megathrust coupling, between a nearly fully locked (90% coupling) segment to the east of the Shumagin Islands, and a nearly creeping segment to the west (Fournier and Freymueller, 2007; Li and Freymueller, 2018; Elliott and Freymueller, 2020; Drooff and Freymueller, 2021) (Fig. 1). Mechanical modeling suggests that the 2021 Chignik earthquake caused a stress increase in a narrow (~45 km) segment close to Chirikof Island and eastward (Elliott et al., 2022). These observations suggest that the region surrounding Chirikof Island and including the Chirikof fault, could be primed for seismic rupture and therefore poses a significant seismic hazard.

Satellite images and digital elevation models indicate that the Chirikof Fault exhibits a fault scarp that traverses for 9 km along the entire island (Fig. 2). The scarp's sharp morphology, evidence for offset streams (e.g. active water and sediment ponding against the scarp), and exceptional preservation suggest that the Chirikof Fault likely hosted Holocene activity. Therefore, it requires a better understanding of its seismic-tsunami hazard potential. Tsunami deposit records on Chirikof Island suggest that a possible surface rupture due to local faults, like the Chirikof Fault, in an 1880 earthquake might have triggered a tsunami (Nelson et al., 2015). And, the Chirikof Fault may behave similarly to the upper plate normal fault that ruptured co-seismically during the 2011 Tohoku-Oki Earthquake, which substantially contributed to the generation of the resultant tsunami (Mw 9.0) (Tsuji et al., 2011; Tsuji et al., 2013; McKenzie and Jackson, 2012). The activity of an individual splay fault, like the Chirikof Fault, can also affect the seismic-tsunami hazard of other structures within the wedge. For example, a fully locked Chirikof Fault over several earthquake cycles implies a strongly stressed state of the backstop splay fault at a shallower depth trench-ward because both the 2020 and 2021 thrusting events only ruptured the deeper sections (~15-45 km deep) of the megathrust (Crowell and Melgar, 2020; Liu et al., 2020; Xiao et al., 2021; Liu et al., 2022).

Apart from addressing seismic-tsunami hazard, a better understanding of the geometry, kinematics, evolution, and seismic activity of the Chirikof Fault is also important for assessing the stress state in the wedge and in understanding how the upper plate deforms in response to the along-strike changes in mechanical properties of the subduction interface. Upper-plate faults, as significant mechanical heterogeneities in the wedge, can affect strain accommodation over multiple seismic cycles (e.g. Wang et al., 2019; McKenzie and Jackson, 2012). The activity of these splay faults provides critical constraints on estimates of mechanical properties within the wedge (e.g. Cubas et al., 2013). In addition to along-strike changes in megathrust coupling, seismic reflection profiles image decreases in the thickness of subducted sediment from the Semidi segment to the Shumagin segment, along with changes in elevated pore pressure at the wedge base, and an increase in roughness of the lower plate (Li et al., 2018). A coincident change in the orientation of the fabrics in the subducting plate is thought to affect subduction zone seismicity by contributing to along-strike changes in faulting and hydration of the subducting and lower plate bending (Shillington et al., 2015; Lynner, 2021).

2. Geology of the Chirikof Island and the Chirikof Fault

Previous geologic mapping recognized three principal formations on the island (Moore, 1962): (1) the Sitkinak Formation (Tsk), a tightly folded and faulted conglomerate, sandstone, and shale unit of Oligocene age; (2) the Tugidak Formation (QTtg), a gently dipping siltstone unit of Pliocene age; and (3) Qg, an uplifted glacial-marine gravel and silt unit of Pleistocene age (Fig. 2).

The Sitkinak Formation underlies the southern three-quarters of Chirikof Island. Our field survey area is located within the region containing the Sitkinak Formation. Bedrock only outcrops along the sea cliff, and most of the surface slope is covered and vegetated. The strata are strongly faulted and folded and steeply dipping. Bathymetry data adjacent to the island show bedding patterns offshore (Fig. 2). To the northeast of the island, the bathymetry data shows pairs of folds and probably faults within the Sitkinak formation. The deformation style is similar to the Sitkinak Formation in the Kodiak Islands area, which has been interpreted as off-scraped sediment from the subducting plate.

The Tugidak marine sandy siltstone unconformably overlies the strongly deformed Sitkinak Formation (unpublished report by Moore, refer to the supplementary file of Nelson et al., 2015). It is primarily mapped in the northern part of Chirikof Island and is separated from the Sitkinak Formation by a NE-SW striking fault that is not well studied (Fig. 2). On the northernmost part of the island, the Tugidak Formation is covered by Quaternary glacial-marine deposits. South of the fault in the eastern coastal area, approximately 2 km^2 of the Tugidak Formation is mapped unconformably overlying the Sitkinak Formation. The bathymetry data northwest and northeast of Chirikof Island shows the bedding patterns offshore, which exhibit anticline-syncline pair. In the northwest of the island, the bedding pattern exhibits an offset approximately along the core of the anticline, which suggests the anticline-syncline pair is a result of folding at the tip of a mostly blind fault-propagation reverse fault (Fig. 2).

The active Chirikof Fault strikes approximately parallel with the strongly faulted and folded high-angle beds of the Sitkinak Formation and is expressed as a linear northwest-facing scarp that offsets an overall southeast-facing slope covered by regionally extensive glacial till. In the study area in the southwestern part of the island, the bedrock exposure of the fault zone is only seen along the southwestern sea cliff. The fault zone involves the sandstone of the Sitkinak Formation. Kinematic indicators such as slikenlines and the Riedel shear fractures accompanying the fault surfaces indicate the Chirikof Fault is a pure normal fault (Fig. 3). A portion of the normal sense slip is also accommodated by bedding-parallel slip along high-angle thin beds (Fig. 3). Glacial till on the surface overlaying the Sitkinak Formation is also offset by the fault. The glacial till is characterized by a pebble-cobble-rich unit at the bottom and a silt-rich unit in the upper part (Figs. 2 and 3f).

3. Tectonic Geomorphology

The Chirikof fault scarp cuts through the island and can be recognized in 2-m resolution digital elevation models and in aerial images. The interaction between fault and topography (i.e. the trace of the fault scarp) suggests an overall 224/64 (strike/dip, right-hand rule) fault surface

orientation. In the western part of the island, field sightings of the fault trace across the topography suggest the dip ranges 55-64 degrees. Bathymetric data suggest the topographic scarp on the surface continues offshore southwestward, although it is unclear how far southwestward the fault extends. The northeast offshore extension is not clear in the bathymetry data near offshore, and the anticline-syncline pattern of the Tugidak Formation 4 km from the fault trace on the island does not show an observable offset. This may suggest only a small amount of, or zero, fault offset further offshore northeast of the island.

On the island, we conducted a field survey along the southwesternmost ~ 2 km segment of the fault trace (Fig. 2). We refer to the fault scarp surface as the northwest-facing surface along the fault that cuts the overall southeastern-facing hillslope in our study area. Along the surveyed segment, the fault scarp exhibits an increased degradation from the southwest to the northeast. The scarp in the southwest segment is clear and high, whereas the scarp in the northeast segment is degraded and low (Fig. 3). We collected dGPS high-resolution elevation data along scarp-perpendicular transects to document fault morphology and offset and their along-strike changes along-strike changes (section below).

Drainages and sediments on the fault-cutting southeast-facing slope are often ponded against the fault scarp on the uphill downthrow side (Figs. 4 and 5). A series of transverse channels across the fault scarp do not show consistent lateral deflection, suggesting neglectable or low amounts of strike-slip displacement of the active fault (Figs. 2 and 4). This observation is consistent with the kinematic indicators of bedrock structures we observed that outcrop along the sea cliff at the southeastern end of the fault trace on the island (Fig. 3). At the intersections between the active channels and fault scarp, remnant inset paleochannels at several localities suggest that the fault scarp reflects more than one surface-rupturing earthquake along the Chirikof Island Fault (Figs. 4 and 5). At two localities, we also collected dGPS data of the fault scarp crest and short scarp-normal transects to document the fault-scarp morphology and the offset transverse channel morphology. In both cases, the paleochannels preserve fault scarps of several tens of centimeters high (Fig. 5). We further selected one locality and conducted a detailed systematic survey, including a drone flight to collect high-resolution images for producing a DEM using photogrammetry, drilling Quaternary sediment cores, and collecting Quaternary dating material for radiocarbon dating.

4. Detailed Geomorphology and Paleoseismology Survey

4.1 High-resolution dGPS fault scarp survey

To quantify surface offset and document the fault-scarp morphology, we conducted dGPS high-resolution fault scarp surveys in the western part of the fault in our surveyed area (Fig. 2e). At different locations along the fault, we collected cm-level GPS coordinates of surface points along strike-normal profiles across the fault scarp. The data was collected using two Trimble Geo 7X Handheld GNSS Systems with a Zephyr 3 Rover Antenna. One system was used as a base station and the other was used for surveying. Differential GPS data processing was conducted using the Trimble GPS Pathfinder Office software. We selected survey profiles along interfluves, trying to avoid significant modifications from erosion or deposition in the ponded areas in the hanging wall against the fault scarp. We selected topographic profiles longer than 30 m on both sides of the scarp to calculate throw, heave, vertical separation, and displacement

across the fault by assuming the topography on each side of the fault scarp represent the same geomorphic surface of post-glacial till (Fig. 6). We used a MATLAB code to conduct the analysis following the method in Morell et al. (2017). The code simulates the best-fit surfaces of the hanging wall and footwall and calculates vertical separations based on the simulated best-fit surfaces. The code further calculates throw, heave, and displacement based on user-defined fault location and dip. The uncertainties are calculated based on the uncertainties of surface regression and the user-defined possible ranges of fault-trace location and fault dip. Several short profiles are also reported here to show the fault scarp morphology, but the offset calculation is not conducted.

The calculated vertical separation ranges from 4.02 ± 0.05 m (Profile 12) to 9.52 ± 0.15 m (Profile 7). Assuming a fault dip of 60 ± 4 results in total fault displacement estimates ranging from 3.87 ± 0.05 m to 9.23 ± 0.16 m (Fig. 6). We find that although the fault scarp is more degraded in the northeastern part of the study area (Figs. 3, 6 and 7, Profiles 6-10), the calculated displacement is similar to, if not larger, than the southwestern part (Profiles 1-5, 11-13). The largest fault displacement estimate of 9.23 m is obtained from profile 7 in the northeastern part of the survey area. Profile 6 near profile 7 in the northeastern part yields a fault slip estimation of 6.07 m. Profiles in the southwestern part of the survey area yield estimates of fault displacement ranging from 3.87 m to 7.37 m and half of these 8 profiles yield fault-slip estimates larger than that of profile 6 in the northeast. The fault-scarp heights in profiles 8-10 in the northeastern are are less than 1 meter tall and reach as low as several centimeters (Here the fault-scarp height means the elevation change between the lowest and the highest points of the northwest-facing scarp surface that cuts the overall southeast-facing pre-faulting ground surface). But the profiles are too short and cannot be used for surface reconstruction. The apparent low fault scarp in the northeastern part represented by profiles 6-10 is likely due to degradation as indicated by the fault scarp morphology (Figs. 6 and 7).

We also collected dGPS data along the fault-scarp crest and scarp-normal transects at the two localities where active channels intersect the fault scarp (Figs. 5 and 7). One locality is the area where we conducted the detailed survey and we collected 16 sediment cores in the hanging wall (Fig. 4). The scarp-normal topography profile Pcore-1 is along one of the coring transects. The Pcore-2 is a profile along the fault crest across the active channel. The other locality is between profiles 11 and 12 (Figs. 2, 4 and 5). The Px-1 and Px-2 are the scarp-crest profile and scarp-normal profile, respectively. The Px-2 scarp-normal profile crosses the remnant of the paleochannel surface between the local active channels and exhibits offset of the paleochannel surface (Figs. 4 and 5). The two scarp-crest profiles (Pcore-2 and Px-1) of these two localities show the fault scarp of the slope surface and the paleochannel remnants are incised by active channels (Figs. 5 and 7).

4.2 Geomorphic mapping and Photogrammetry of the detailed survey area

We used a drone to take pictures of the surveyed area and used photogrammetry to construct three-dimensional models. The 3D model construction of the detailed survey area was conducted using Agisoft software with 12 ground control points. The coordinates of the 12 ground control points were collected using dGPS. With the high-resolution digital elevation model and drone image derived from the drone photos, we mapped the geomorphology of the

survey area (Fig. 4ab). The survey area shows the interaction between an active drainage system and the fault scarp. The fault scarp is clearly shown on the hillshade map of the digital elevation model and the contour pattern (Fig. 4a). The drone image map shows the changes in surface moisture and vegetation (Fig. 4b). The surface moisture is reflected in the color and the vegetation. The exposures of quaternary deposits below the vegetated surface show similar characteristics of the glacial till overlying the bedrock observed at the seacliff (Fig. 3f). The glacial till is exposed in both hanging wall and footwall and is up to >1.2 m thick in this mapping area (Fig. 4). Similar glacial till sections are observed in our two sampling pits, one observation pit, and several observation sections we dug in the southeastern part of the island.

To investigate the rupture history of the fault, in the detailed survey area, we used a hand-auger to core into Quaternary sediment ponded in the hanging wall near the fault and to collect radiocarbon dating samples. The 16 collected sediment cores were distributed and aligned along two scarp-normal transects and one scarp-parallel transect in the hanging wall (Fig. 4b). The two scarp-normal transects straddle the ponded sediment in the hanging wall and fault scarp. The depth of the cores varied from 0.3 m to 2.0 m and are generally deeper than 1 m. Details of the sediment cores are presented in Figure 8. The sediment extracted from the cores is mainly silt-rich fine-grain sediments. Color varies depending on the percentage of silt, clay, organic matter, and moisture. The changes in sediment content are gradual and no significant changes in grain size were observed. We interpret that the sediment is mostly recycled silt-rich content of hillslope sediment derived either from underlying bedrock or glacial till. No clear sediment record of earthquakes is recognized from the cores.

4.3 Quaternary dating and results from coring

To better understand the timeframe of the ponded sediments, we collected 7 radiocarbon samples from the sediment cores and 3 radiocarbon dating samples from two sampling pits. The radiocarbon dating materials are primarily organic matter and sedges. Ten samples in total were analyzed. We encountered a relatively continuous tephra layer that appears in several cores with a strawberry color. We collected two tephra analysis samples from cores CFM1-15 and CFM1-16 for analysis.

Presently, the results of the tephra analyses are pending. The radiocarbon dating results are shown in Table 1 and Figure 9, and the samples are also annotated on the core images (Fig. 8). Five of the radiocarbon ages are modern before calibration. We used OxCal software (Ramsey, 2009) to calibrate the radiocarbon dating results. The IntCal20 Northern Hemisphere Radiocarbon Age Calibration Curve (Reimer et al., 2020) and Bomb21NH1 curve (Hua et al., 2022) are used for calibrating the raw ages that are older than “modern” and “modern” ages, respectively. The raw ages of Samples CF23C14-08 and CFM1-15-1 are close to modern; we also used curve Bomb21NH1 to conduct calibration. The two oldest calibrated ages (4847-4723 BC and 4050-3947 BC) are from core CFM1-16 at the depths of 182 cm and 191 cm.

5. Discussion

5.1 Regional Tectonic history and the formation of the Chirikof Fault

The extensive folding and faulting structures in the Sitkinak Formation may mostly represent the strong deformation it experienced as it offscapred from the subduction plate and accreted to the forearc wedge during the Oligocene. This process and similar deformation style have been documented for the Sitkinak Formation exposed in the trenchward coastal area of the Kodiak Islands northeastward along strike (Moore and Allwardt, 1980). The unconformity between the Sitkinak Formation and the Tugidak Formation indicates the Sitkinak Formation in this area experienced erosion after its accretion to the forearc wedge, followed by subsidence and the deposition of the Tugidak Formation. The formation of the unconformity can be regionally correlated with the record in the Kodiak Islands area, where the unconformity between the strongly deformed Sitkinak Formation and the gently deformed Miocene strata are observed both onshore and offshore in the coastal area (Clendenen et al., 1992; Fisher and Holmes, 1980; Moore and Allwardt, 1980). In the Chirikof area, this unconformity can also be observed on a legacy seismic image ~10 km northeast of the island (Fig. 10). The seismic image in Figure 10 was collected in 1983 and can be accessed from the National Archive of Marine Seismic Surveys hosted by the USGS (Dataset ID: B-66-83-AK). The annotations in the figure show our interpretation.

After the deposition of the Tugidak Formation, the area experienced gentle shortening as indicated by the broad anticline and syncline pair of the Tugidak Formation and a thrust fault locally developed in the core of the anticline (Fig. 2). This episode of thickening uplifted the area to a subaerial environment, and after a period of erosion, the area subsided and received younger sediments again. This process is indicated by the second unconformity on the seismic image. The gently folded strata below the unconformity can be correlated with the Tugidak Formation. The young sediment above the unconformity is currently mostly intact, with only several small open folds of wavelength of ~1 km in the northwestern part and is likely Pleistocene-Holocene sediment (Fig. 10).

The active Chirikof Fault developed in the Sitkinak Formation. Because it strikes parallel with the older structures associated with offscarping and accretion of the Sikinak Formation at a high dip angle similar to bedding and records of bedding parallel slip are observed in the fault zone, we suggest that the fault may have developed by reactivating preexisting faults or weak units in beds within the Sitkinak Formation. The young, presumably Holocene sediment unconformably overlying the gently folded Tugidak Formation on the seismic images only shows a small amount of shortening deformation in the northwestern portion of the profile.

The observed bedrock structures, clear fault scarp, offset paleochannels, and ponded active drainages in our study area all indicate that the Chirikof Fault is a Quaternary-active normal fault and has accommodated recent extension. Therefore, these observations overall suggest a tectonic transition from shortening to active extension that may have occurred in the Pleistocene-Holocene. The seismic image northeast of the island does not show a clear normal sense offset of the gently folded Tugidak Formation or the younger Holocene sediment (Fig.10), and the bathymetry data to the northeast of the island also does not show a clear offset in the pattern of surface bedding (Fig. 2). These observations suggest the active normal fault may tip out close to the island offshore to the northeast or accommodate only unobservable slip to the northeast of the island.

5.2 Paleoseimology of the Chirikof Fault

It is unclear how many earthquakes have been hosted by the Chirikof Fault that are recorded by the scarp. Several lines of evidence suggest the fault may have hosted more than one surface-rupturing earthquake since the last glacial maximum at ~12 ka. The low scarps of the paleochannel surfaces suggest that the paleochannels may have formed during the time interval between the last earthquake rupture and earlier rupture events (Fig. 5). The different degradation extents of the fault scrap along the strike may also suggest that different segments of the fault may have ruptured at different times if the degradation extent is proportional to the age of recent surface ruptures. There are no clear abrupt changes in the sediment record observed in the cores in our survey area, which may support that the fault scarp formed by incrementally accumulating many low-magnitude displacements over many earthquakes rather than by one earthquake.

Moreover, our surface construction results in as much as 6-9 m total fault displacement, which, if caused by one earthquake, requires an earthquake of magnitude of 7.2-7.4 based on the magnitude-displacement scale relationship (Wells and Coppersmith, 1994; Wesnousky, 2008). Even if the total surface offset is caused by 3-4 earthquakes, i.e., fault displacement of 2-3 meters in each earthquake, the earthquakes could be ~M7 events. But there is no such a major normal-sense earthquake recorded in this region. Although depositional records of tsunamis have been reported from the island, the sources and nature of the triggering earthquakes are unknown (Nelson et al., 2015).

We also examined Interferometric Synthetic Aperture Radar (InSAR) data of the island over the interval affected by the 2021 Mw 8.2 Chignik earthquake in the nearby subduction zone segment (Fig. 11). The InSAR image is generated from processing two descending scenes of Sentinel-1 data obtained 10 days before and 2 days after the earthquake on July 19, 2021 and July 31, 2021, respectively, on the Vertex platform of the Alaska Satellite Facility. The vertical displacement map is generated from the unwrapped differential phase measurements under the assumption that the displacement is entirely in the vertical direction. We find the vertical displacement map exhibits an observable discontinuity across the Chirikof fault, although the data uncertainty is large compared with the discontinuity (Fig. 11). Several cross-fault profiles of the vertical displacement show that the discontinuity represents an abrupt change of as much as ~2 cm in displacement across the fault, which also suggests the accumulation of low-magnitude displacements may have contributed to the formation of the fault scarp.

The oldest radiocarbon ages at the bottom of the cores may provide a lower limit on the initial formation of the fault scarp. The average slip rate of the fault will be estimated after the pending tephra analysis results are obtained.

5.3 Along-strike forearc tectonic setting change

Several lines of evidence suggest the Chirikof Fault could represent one of a series of regionally extensive Holocene-active upper plate fault structures across this portion of the Alaska subduction zone. In the Shumagin Islands segment to the southwest, a landward-dipping normal splay fault is identified on seismic reflection profiles ~80 km arcward from the trench (Bécel et al., 2017; von Huene et al., 2019), at an approximately correspondent structural location as the

Chirikof Fault (~ 110 km from the trench in a slightly wider wedge) (Fig. 1). Studies suggest that the normal splay fault in the Shumagin segment developed by reactivating a suture between terranes accreted to the Alaska forearc and the suture extends for 300 km along the margin (Shillington et al., 2022; von Huene and Miller, 2024). To the northeast of the Semidi segment, active upper-plate structures in the inner-wedge are also reported at a similar structural location (e.g. Carver et al., 2008; Liberty et al., 2013; Haeussler et al., 2015; Ramos et al., 2022) (Fig. 1). In the Kodiak and Prince William Sound segments, thrust-sense splay fault systems are identified from seismic reflection profiles and is interpreted to have ruptured during the tsunamigenic 1964 M_W 9.2 Great Alaska earthquake (Liberty et al., 2013; Haeussler et al., 2015; Liberty et al., 2019; Ramos et al., 2022) and these active thrust faults may have started several million years ago (Haeussler et al., 2015; Fan et al., 2023). The offshore active thrust fault scarps associated with the Kodiak Shelf Fault System offshore of the Kodiak Islands extend to about 100 km northeast of Chirikof Island. Our survey in this study suggests that Chirikof Island experienced a change from shortening deformation to the activation of the extensional normal faulting deformation probably very recently in the Pleistocene-Holocene, and the fault on the island may tip out not far from the island offshore to the northeast. Therefore, Chirikof Island may represent an along-strike transition between active shortening and active extension.

The driving force of the formation of the Chirikof Fault is unclear, but it is possible that the normal faulting is caused by forearc extensional earthquakes associated with great plate-interface megathrust earthquakes. Extensional earthquakes following a major megathrust earthquake are common in subduction zones, and mechanical models suggest that this extension may be linked to different stress-change processes of different parts in the forearc over seismic cycles (Wang and Hu, 2006). Chirikof Island is approximately located in the region where this process may occur. These extensional earthquakes typically have smaller magnitudes than the major megathrust events and our survey, as discussed above, also suggests that the accumulation of small earthquake ruptures is likely the forming process of the fault scarp. In this case, the main controlling factor for triggering the normal faulting is the stress states and mechanical properties within the wedge over seismic cycles of the Semidi segment, which can be significantly affected by the plate-interface stress state and mechanical properties. This may also explain why the along-strike change from active overall shortening to overall extension in the forearc approximately correlates with the along-strike change in the plate-interface coupling and earthquake patterns. If true, the fault may rupture co-seismically with the megathrust or after great megathrust earthquakes. However, based on the current data, we cannot rule out that the earthquakes occurred during the megathrust interseismic period.

6. Conclusions

We investigated the geometry, surface displacement, and seismic activity of the Chirikof Fault in the southwestern part of the island by conducting geological and tectonic geomorphologic surveys and Quaternary sediment coring, augmented by quaternary dating and offshore bathymetry mapping. We find that the Chirikof Fault is a ~60-degree arcward-dipping normal fault that may have hosted more than one surface-rupturing earthquake and resulted in ~4.0 m to ~9.5 m of vertical separation across a regionally extensive surface of glacial till, which may date to the last glacial maximum. The fault scarp exhibits variations in degradation extent along strike. The fault may have developed by reactivating preexisting structures or weak units

in the strongly deformed Oligocene Sitkinak Formation. The Chirikof Island area experienced a change from a compressional to an extensional setting in the Pleistocene-Holocene. Comparing the geology of the Chirikof Island, including the Chirikof Fault, with the forearc upper-plate structures in adjacent segments of the Alaska subduction zone, we suggest that the Chirikof Island area may represent an NE to SW along-strike transition from active forearc internal shortening to extension.

Project data

The photogrammetry results in this project are stored in Zenodo and publicly available using the URL https://doi.org/10.5281/zenodo.13346470. After all analyses for this project are completed, we will upload and archive other datasets, including dGPS data, dating results, and high-resolution maps. Users can use the same URL to access the data.

Acknowledgment of support

This material is based upon work supported by the U.S. Geological Survey under Grant No. G23AP00287.

Disclaimer

The views and conclusions contained in this document are those of the authors and should not be interpreted as representing the opinions or policies of the U.S. Geological Survey. Mention of trade names or commercial products does not constitute their endorsement by the U.S. Geological Survey.

References

Bécel, A., Shillington, D. J., Delescluse, M., Nedimović, M. R., Abers, Geoffrey A., Saffer, D. M., Webb, S. C., Keranen, K. M., Roche, P.-H., Li, J., and Kuehn, H., 2017, Tsunamigenic structures in a creeping section of the Alaska subduction zone: Nature Geoscience, v. 10, no. 8, p. 609-613, https://doi.org/10.1038/ngeo2990.

Boyd, T. M., and Lerner-Lam, A. L., 1988, Spatial distribution of turn-of-the-century seismicity along the Alaska-Aleutian Arc: Bulletin of the Seismological Society of America, v. 78, no. 2, p. 636-650, https://doi.org/10.1785/BSSA0780020636.

Carver, G., Sauber, J., Lettis, W., Witter, R., Whitney, B., and Freymueller, J., 2008, Active faults on northeastern Kodiak Island, Alaska: Active tectonics and seismic potential of Alaska: American Geophysical Union Geophysical Monograph, v. 179, p. 167-184.

Clendenen, W. S., Sliter, W. V., and Byrne, T., 1992, Tectonic implications of the Albatross sedimentary sequence, Sitkinak Island, Alaska.

Crowell, B. W., and Melgar, D., 2020, Slipping the Shumagin Gap: A Kinematic Coseismic and Early Afterslip Model of the Mw 7.8 Simeonof Island, Alaska, Earthquake: Geophysical Research Letters, v. 47, no. 19, https://doi.org/10.1029/2020gl090308.

Cubas, N., Avouac, J. P., Leroy, Y. M., and Pons, A., 2013, Low friction along the high slip patch of the 2011 Mw 9.0 Tohoku-Oki earthquake required from the wedge structure and extensional splay faults: Geophysical Research Letters, v. 40, no. 16, p. 4231-4237, https://doi.org/10.1002/grl.50682.

Drooff, C., and Freymueller, J. T., 2021, New Constraints on Slip Deficit on the Aleutian Megathrust and Inflation at Mt. Veniaminof, Alaska From Repeat GPS Measurements: Geophysical Research Letters, v. 48, no. 4, https://doi.org/10.1029/2020gl091787.

Elliott, J. L., Grapenthin, R., Parameswaran, R. M., Xiao, Z., Freymueller, J. T., and Fusso, L., 2022, Cascading rupture of a megathrust: Science Advances, v. 8, no. 18, p. eabm4131, https://doi.org/10.1126/sciadv.abm4131.

Fan, S., Morell, K. D., and Fisher, D. M., 2023, Low-Temperature Thermochronology Reveals Paleogene to Recent Exhumation Related to Upper Plate Thrust Faulting above the Downdip Edge of the Seismogenic Zone, Kodiak Island, Alaska Subduction Zone: AGU23.

Fisher, M. A., and Holmes, M. L., 1980, Large-scale structure of deep strata beneath Kodiak shelf, Alaska: GSA Bulletin, v. 91, no. 4, p. 218-224, https://doi.org/10.1130/0016-7606(1980)91<218:Lsodsb>2.0.Co;2.

Fournier, T. J., and Freymueller, J. T., 2007, Transition from locked to creeping subduction in the Shumagin region, Alaska: Geophysical Research Letters, v. 34, no. 6, https://doi.org/10.1029/2006GL029073.

Freymueller, J. T., Suleimani, E. N., and Nicolsky, D. J., 2021, Constraints on the Slip Distribution of the 1938 MW 8.3 Alaska Peninsula Earthquake From Tsunami Modeling: Geophysical Research Letters, v. 48, no. 9, https://doi.org/10.1029/2021gl092812.

Haeussler, P. J., Armstrong, P. A., Liberty, L. M., Ferguson, K. M., Finn, S. P., Arkle, J. C., and Pratt, T. L., 2015, Focused exhumation along megathrust splay faults in Prince William Sound, Alaska: Quaternary Science Reviews, v. 113, p. 8-22, https://doi.org/10.1016/j.quascirev.2014.10.013.

Hua, Q., Turnbull, J. C., Santos, G. M., Rakowski, A. Z., Ancapichún, S., De Pol-Holz, R., Hammer, S., Lehman, S. J., Levin, I., Miller, J. B., Palmer, J. G., and Turney, C. S. M., 2021, Atmospheric Radiocarbon for the Period 1950–2019: Radiocarbon, v. 64, no. 4, p. 723-745, https://doi.org/10.1017/rdc.2021.95.

Johnson, J. M., and Satake, K., 1994, Rupture extent of the 1938 Alaskan earthquake as inferred from tsunami waveforms: Geophysical Research Letters, v. 21, no. 8, p. 733-736, https://doi.org/10.1029/94gl00333.

Li, S., and Freymueller, J. T., 2018, Spatial Variation of Slip Behavior Beneath the Alaska Peninsula Along Alaska-Aleutian Subduction Zone: Geophysical Research Letters, v. 45, no. 8, p. 3453-3460, https://doi.org/10.1002/2017gl076761.

Liberty, L. M., Finn, S. P., Haeussler, P. J., Pratt, T. L., and Peterson, A., 2013, Megathrust splay faults at the focus of the Prince William Sound asperity, Alaska: Journal of Geophysical Research: Solid Earth, v. 118, no. 10, p. 5428-5441, https://doi.org/10.1002/jgrb.50372.

Liberty, L. M., Brothers, D. S., and Haeussler, P. J., 2019, Tsunamigenic Splay Faults Imply a Long-Term Asperity in Southern Prince William Sound, Alaska: Geophysical Research Letters, v. 46, no. 7, p. 3764-3772, https://doi.org/10.1029/2018gl081528.

Liu, C., Lay, T., and Xiong, X., 2022, The 29 July 2021 M-W 8.2 Chignik, Alaska Peninsula Earthquake Rupture Inferred From Seismic and Geodetic Observations: Re-Rupture of the Western 2/3 of the 1938 Rupture Zone: Geophysical Research Letters, v. 49, no. 4, https://doi.org/10.1029/2021gl096004.

Liu, C., Lay, T., Xiong, X., and Wen, Y., 2020, Rupture of the 2020 MW 7.8 Earthquake in the Shumagin Gap Inferred From Seismic and Geodetic Observations: Geophysical Research Letters, v. 47, no. 22, https://doi.org/10.1029/2020gl090806.

Lynner, C., 2021, Anisotropy-revealed change in hydration along the Alaska subduction zone: Geology, v. 49, no. 9, p. 1122-1125, https://doi.org/10.1130/g48860.1.

McKenzie, D., and Jackson, J., 2012, Tsunami earthquake generation by the release of gravitational potential energy: Earth and Planetary Science Letters, v. 345-348, p. 1-8, https://doi.org/10.1016/j.epsl.2012.06.036.

Morell, K. D., Regalla, C., Leonard, L. J., Amos, C., and Levson, V., 2017, Quaternary Rupture of a Crustal Fault beneath Victoria, British Columbia, Canada: GSA Today, p. 4-10, https://doi.org/10.1130/gsatg291a.1.

Moore, J. C., and Allwardt, A., 1980, Progressive deformation of a Tertiary Trench Slope, Kodiak Islands, Alaska: Journal of Geophysical Research: Solid Earth, v. 85, no. B9, p. 4741-4756, https://doi.org/10.1029/JB085iB09p04741.

Nelson, A. R., Briggs, R. W., Dura, T., Engelhart, S. E., Gelfenbaum, G., Bradley, L.-A., Forman, S. L., Vane, C. H., and Kelley, K. A., 2015, Tsunami recurrence in the eastern Alaska-Aleutian arc: A Holocene stratigraphic record from Chirikof Island, Alaska: Geosphere, v. 11, no. 4, p. 1172-1203, https://doi.org/10.1130/ges01108.1.

Ramsey, C. B., 2009, Bayesian Analysis of Radiocarbon Dates: Radiocarbon, v. 51, no. 1, p. 337-360, https://doi.org/10.1017/S0033822200033865.

Ramos, M. D., Liberty, L. M., Haeussler, P. J., and Humphreys, R., 2022, Upper-plate structure and tsunamigenic faults near the Kodiak Islands, Alaska, USA: Geosphere, v. 18, no. 5, p. 1474-1491, https://doi.org/10.1130/ges02486.1.

Reimer, P. J., Austin, W. E. N., Bard, E., Bayliss, A., Blackwell, P. G., Bronk Ramsey, C., Butzin, M., Cheng, H., Edwards, R. L., Friedrich, M., Grootes, P. M., Guilderson, T. P., Hajdas, I., Heaton, T. J., Hogg, A. G., Hughen, K. A., Kromer, B., Manning, S. W., Muscheler, R., Palmer, J. G., Pearson, C., van der Plicht, J., Reimer, R. W., Richards, D. A., Scott, E. M., Southon, J. R., Turney, C. S. M., Wacker, L., Adolphi, F., Büntgen, U., Capano, M., Fahrni, S. M., Fogtmann-Schulz, A., Friedrich, R., Köhler, P., Kudsk, S., Miyake, F., Olsen, J., Reinig, F., Sakamoto, M., Sookdeo, A., and Talamo, S., 2020, The IntCal20 Northern Hemisphere Radiocarbon Age Calibration Curve (0–55 cal kBP): Radiocarbon, v. 62, no. 4, p. 725-757, https://doi.org/10.1017/rdc.2020.41.

Shillington, D. J., Bécel, A., Nedimović, M. R., Kuehn, H., Webb, S. C., Abers, G. A., Keranen, K. M., Li, J., Delescluse, M., and Mattei-Salicrup, G. A., 2015, Link between plate fabric, hydration and subduction zone seismicity in Alaska: Nature Geoscience, v. 8, no. 12, p. 961-964, https://doi.org/10.1038/ngeo2586.

Shillington, D. J., Bécel, A., and Nedimović, M. R., 2022, Upper Plate Structure and Megathrust Properties in the Shumagin Gap Near the July 2020 M7.8 Simeonof Event: Geophysical Research Letters, v. 49, no. 2, https://doi.org/10.1029/2021gl096974.

Tsuji, T., Ito, Y., Kido, M., Osada, Y., Fujimoto, H., Ashi, J., Kinoshita, M., and Matsuoka, T., 2011, Potential tsunamigenic faults of the 2011 off the Pacific coast of Tohoku Earthquake: Earth, Planets and Space, v. 63, no. 7, p. 58, https://doi.org/10.5047/eps.2011.05.028.

Tsuji, T., Kawamura, K., Kanamatsu, T., Kasaya, T., Fujikura, K., Ito, Y., Tsuru, T., and Kinoshita, M., 2013, Extension of continental crust by anelastic deformation during the 2011 Tohoku-oki earthquake: The role of extensional faulting in the generation of a great tsunami: Earth and Planetary Science Letters, v. 364, p. 44-58, https://doi.org/10.1016/j.epsl.2012.12.038.

von Huene, R., Miller, J. J., and Krabbenhoeft, A., 2019, The Shumagin seismic gap structure and associated tsunami hazards, Alaska convergent margin: Geosphere, v. 15, no. 2, p. 324-341, https://doi.org/10.1130/ges01657.1.

von Huene, R., and Miller, J. J., 2024, Collision structures of the Prince William terrane and Chugach terrane docking along the Shumagin and Unimak convergent margins, Alaska, USA: Geosphere, https://doi.org/10.1130/ges02757.1.

Wang, K., Brown, L., Hu, Y., Yoshida, K., He, J., and Sun, T., 2019, Stable Forearc Stressed by a Weak Megathrust: Mechanical and Geodynamic Implications of Stress Changes Caused by the M = 9 Tohoku-Oki Earthquake: Journal of Geophysical Research: Solid Earth, v. 124, no. 6, p. 6179-6194, https://doi.org/10.1029/2018JB017043.

Wang, K., and Hu, Y., 2006, Accretionary prisms in subduction earthquake cycles: The theory of dynamic Coulomb wedge: Journal of Geophysical Research: Solid Earth, v. 111, no. B6, https://doi.org/10.1029/2005jb004094.

Wells, D. L., and Coppersmith, K. J., 1994, New empirical relationships among magnitude, rupture length, rupture width, rupture area, and surface displacement: Bulletin of the Seismological Society of America, v. 84, no. 4, p. 974-1002, https://doi.org/10.1785/bssa0840040974.

Wesnousky, S. G., 2008, Displacement and Geometrical Characteristics of Earthquake Surface Ruptures: Issues and Implications for Seismic-Hazard Analysis and the Process of Earthquake Rupture: Bulletin of the Seismological Society of America, v. 98, no. 4, p. 1609-1632, https://doi.org/10.1785/0120070111.

Xiao, Z., Freymueller, J. T., Grapenthin, R., Elliott, J. L., Drooff, C., and Fusso, L., 2021, The deep Shumagin gap filled: Kinematic rupture model and slip budget analysis of the 2020 Mw 7.8 Simeonof earthquake constrained by GNSS, global seismic waveforms, and floating InSAR: Earth and Planetary Science Letters, v. 576, https://doi.org/10.1016/j.epsl.2021.117241.

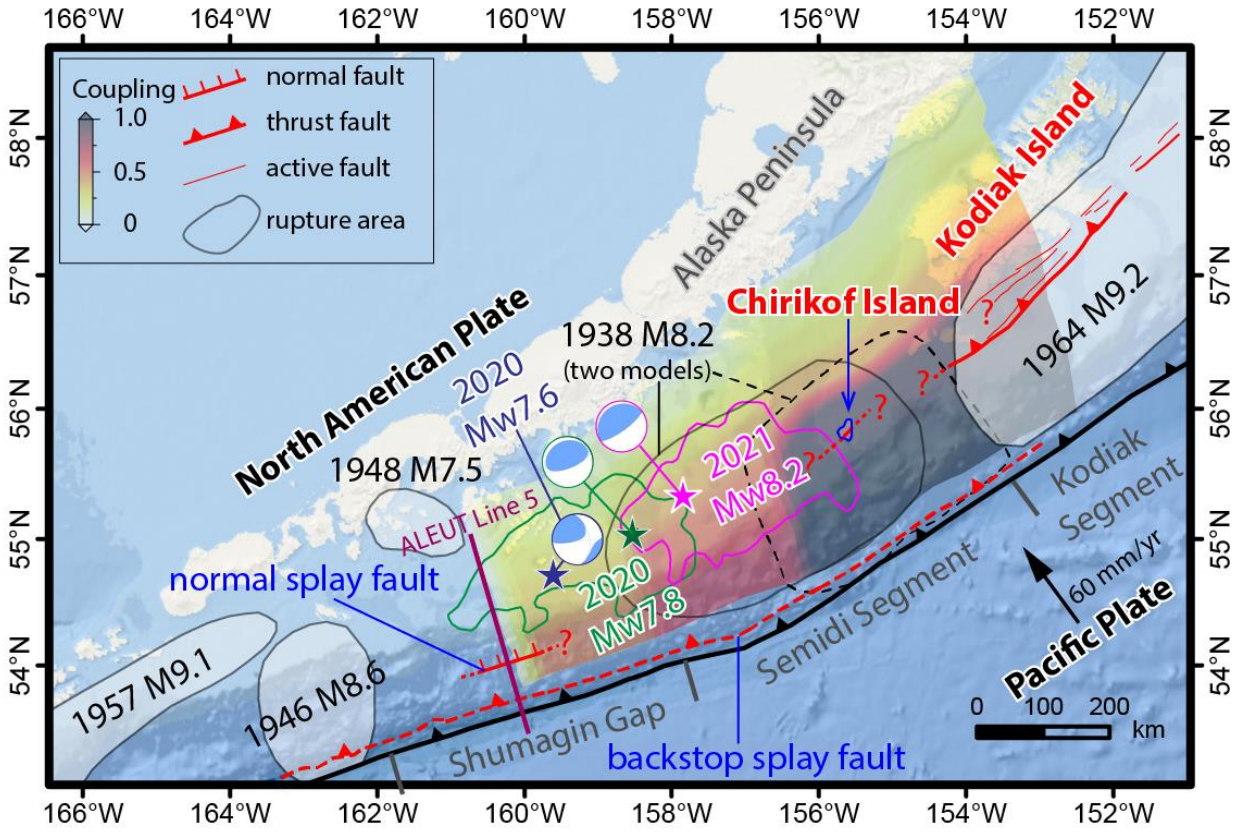

Fig. 1 A map of rupture areas of large earthquakes (Davies et al., 1981; Freymueller et al., 2021; Liu et al., 2022) and major active forearc faults (compiled and inferred from Carver et al., 2008; Bécel et al., 2017; von Huene et al., 2021; Ramos et al., 2022) in the Alaska subduction zone. Subduction interface coupling data is from Li and Freymueller (2018). A large-scale arcward dipping normal fault on the ALEUT Line 5 seismic profile is reported by Bécel et al. (2017).

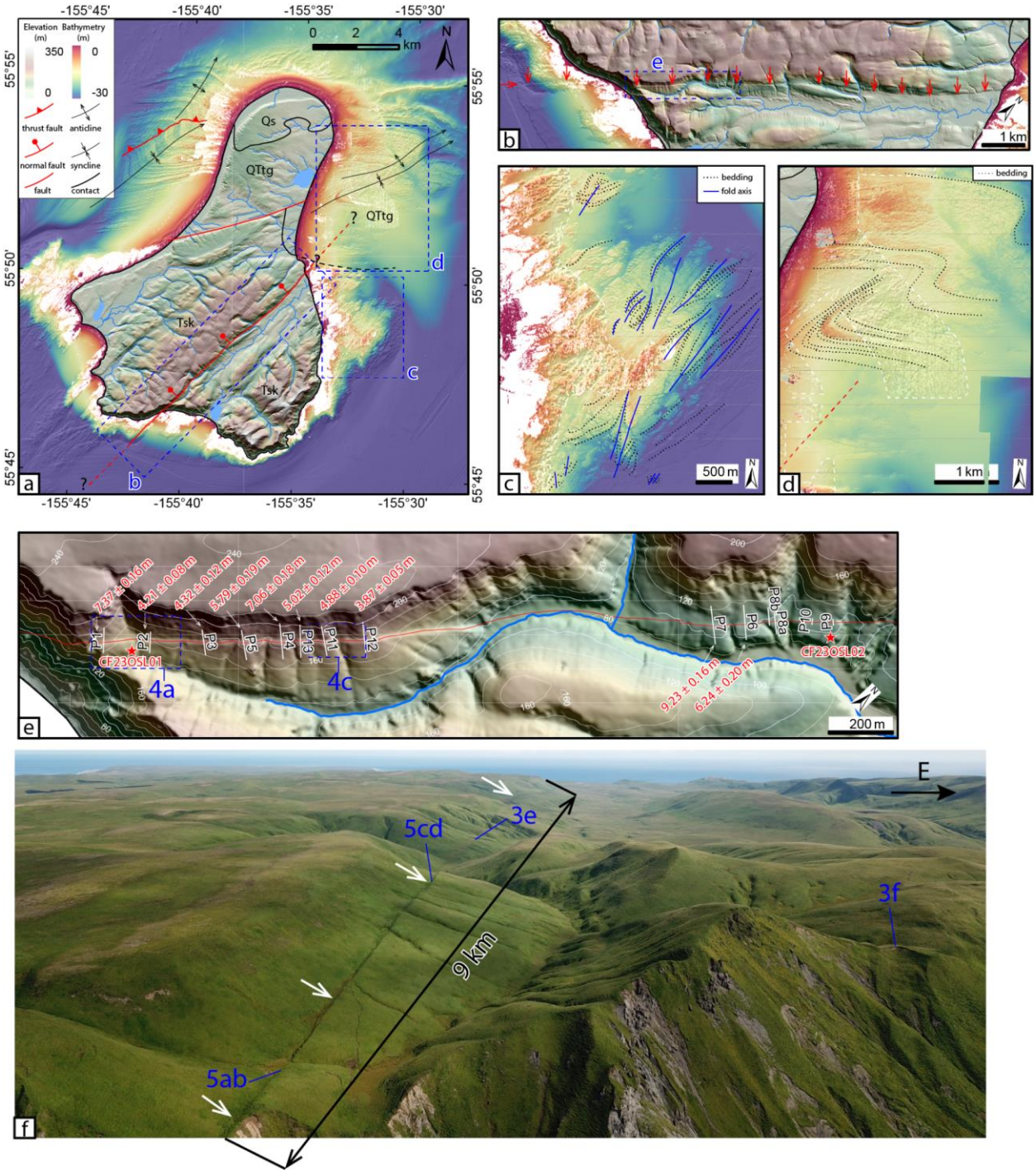

Fig. 2 (a) Geology and elevation-bathymetry map of the Chirikof Island area; (2) Elevation map that shows the Chirikof Fault. Red arrows point to the location of the fault scarp; (c-d) two bathymetry maps that show details of bedding patterns east of Chirikof Island; (e) Elevation map of the western part of the fault area with fault slip estimates based on dGPS data profiles normal to the fault scarp; (f) A drone photo shows the fault scarp in the field.

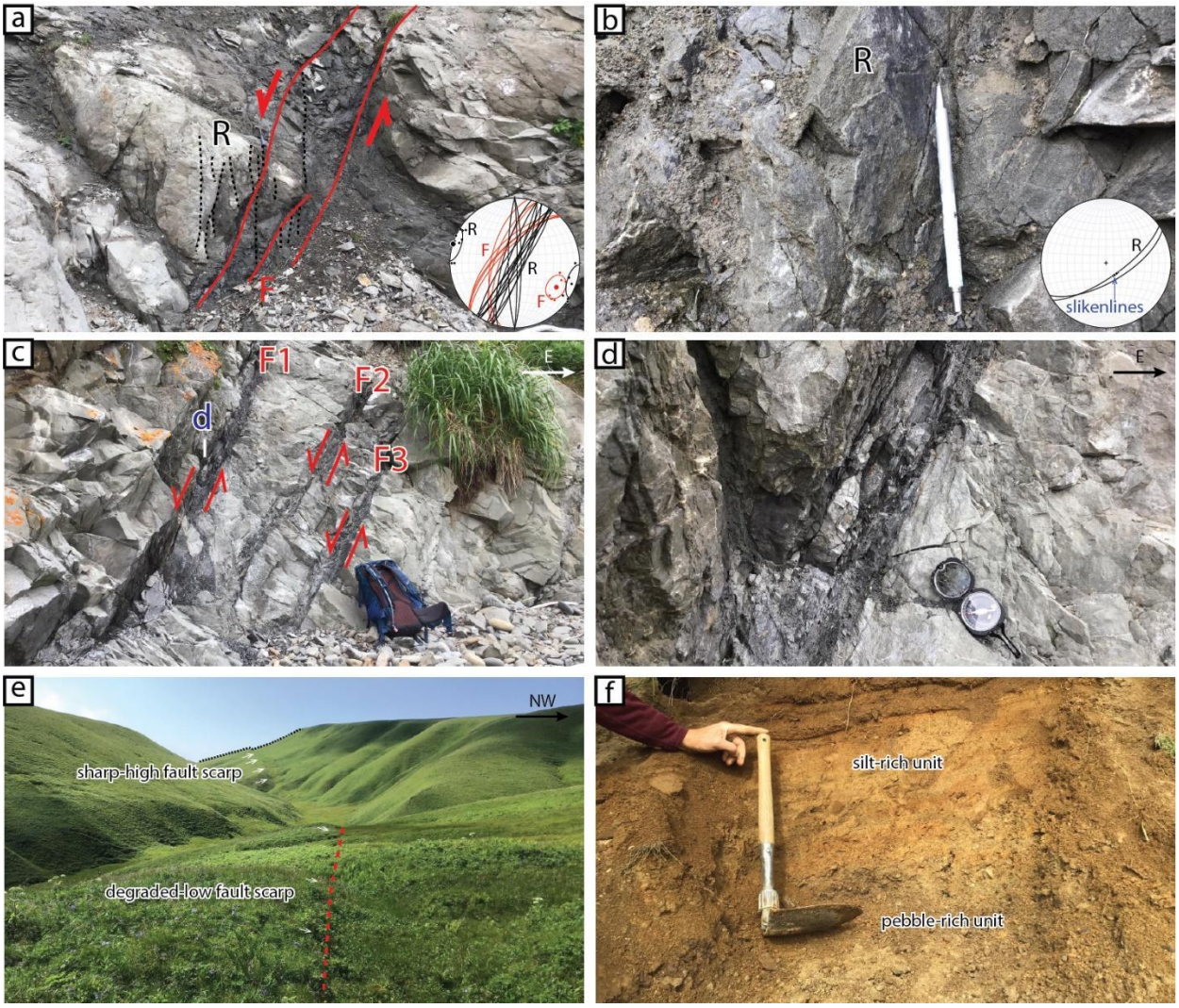

Fig. 3 (a-d) Bedrock structures in the Chirikof Fault zone. R – Riedel shear fractures; (e) A field photo of the fault scarp that shows the along-strike change in the fault-scarp morphology; (f) A photo of the glacial till blanketing the bedrock. Locations of the photos e and f are shown in Fig 2f.

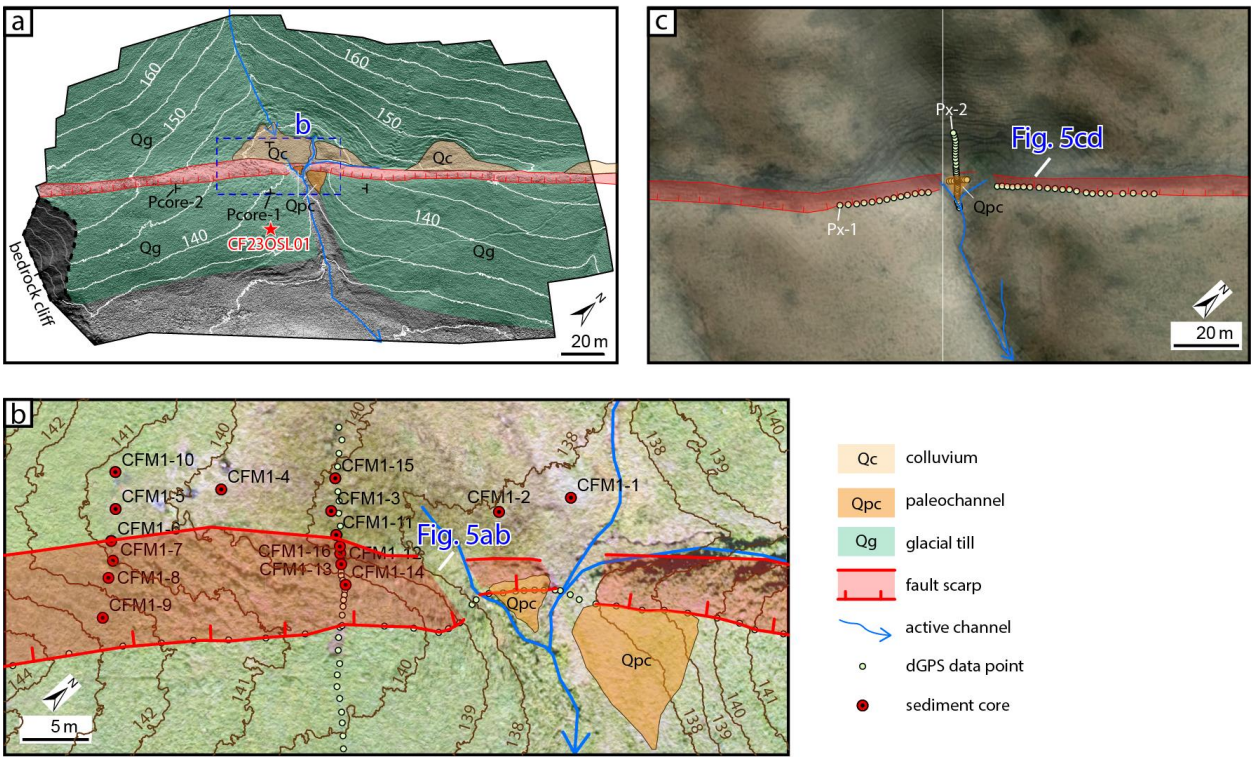

Fig. 4 (a) A detailed geomorphic map of the survey area; (b) A satellite image of one channel-fault intersection; (c) The drone-image map shows locations of quaternary sediment cores and geomorphic features at the intersection of a channel-fault intersection. Basemaps of (a) and (c) are generated from drone photos by photogrammetry. The map extents of (a) and (b) are shown in Fig. 2e.

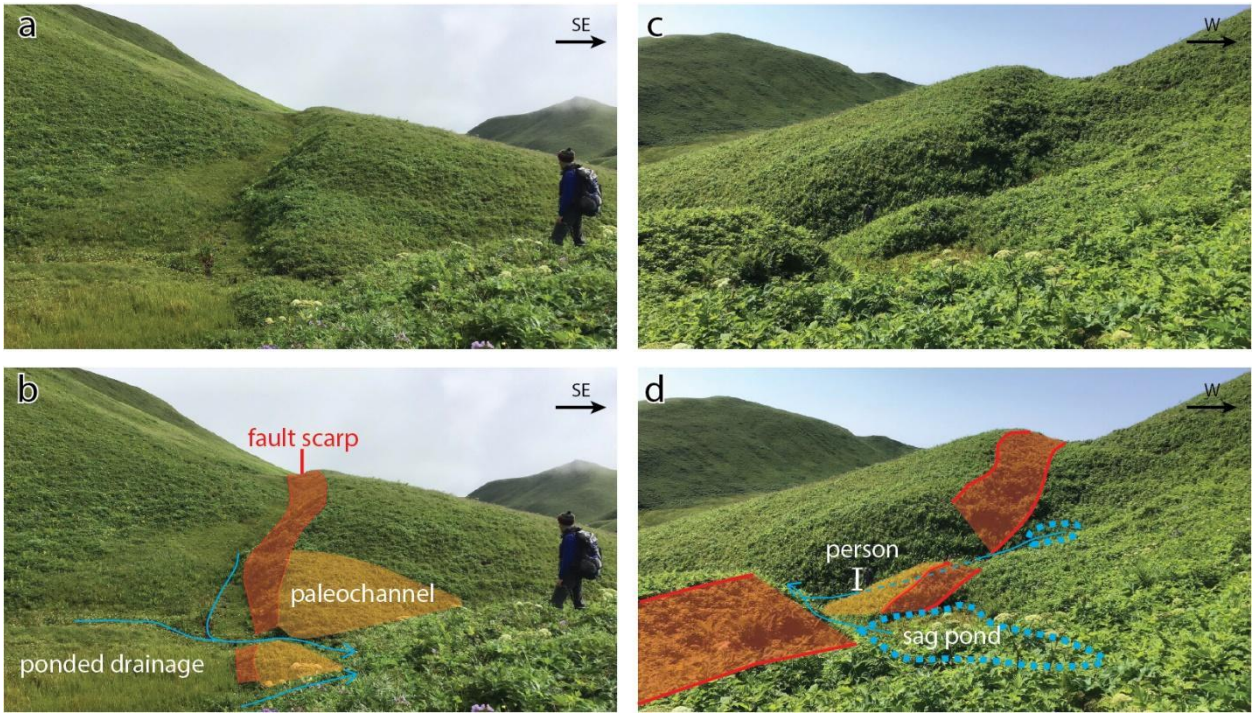

Fig. 5 Field photos and geomorphological interpretation of two channel-fault intersection localities. The locations and maps of them are shown in Figs. 2f and 4.

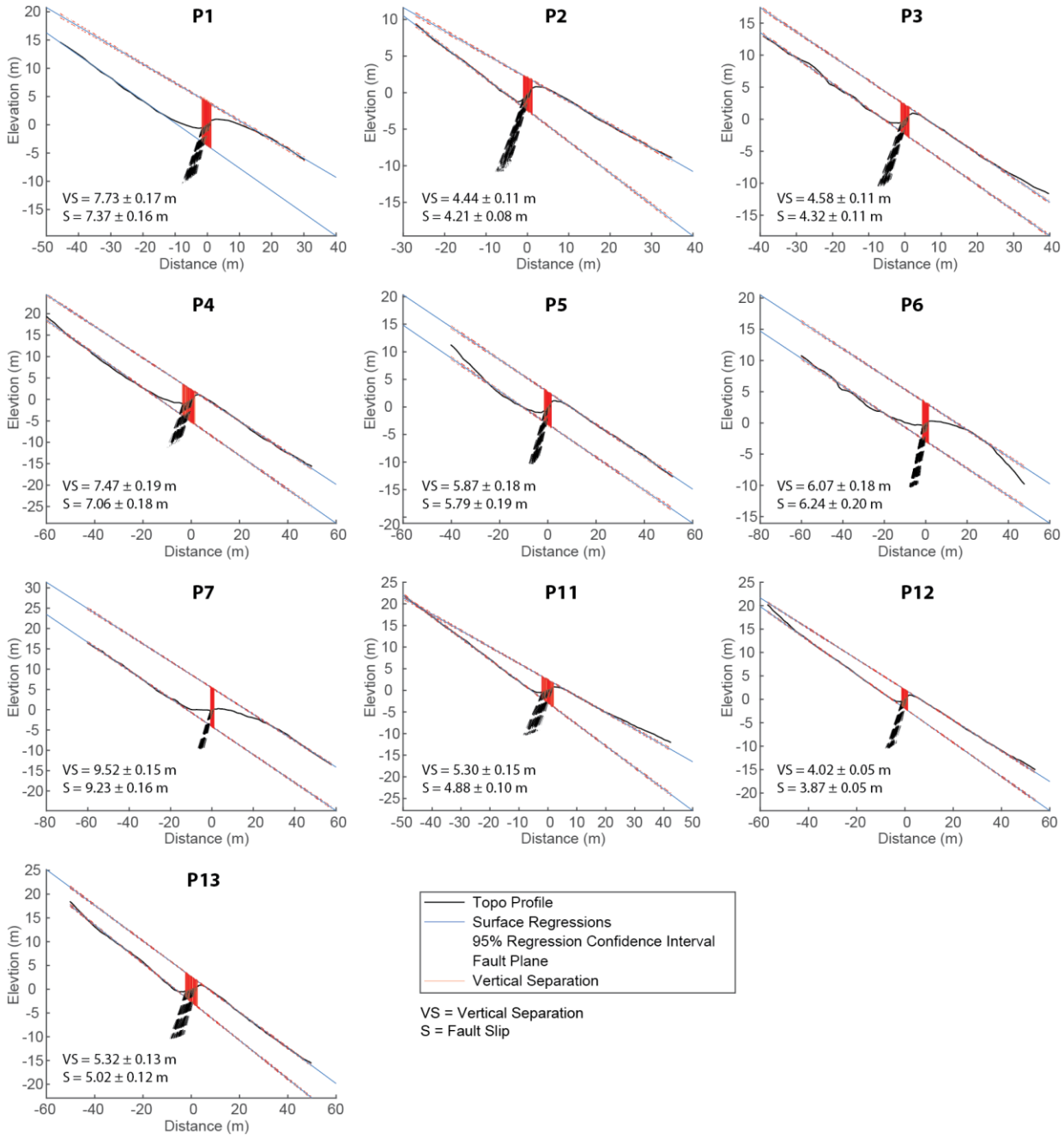

Fig. 6 Topographic profiles across the Chirikof Fault and fault vertical separation estimations. Topographic profile data are from our dGPS survey and the profile locations are shown on Fig. 2e.

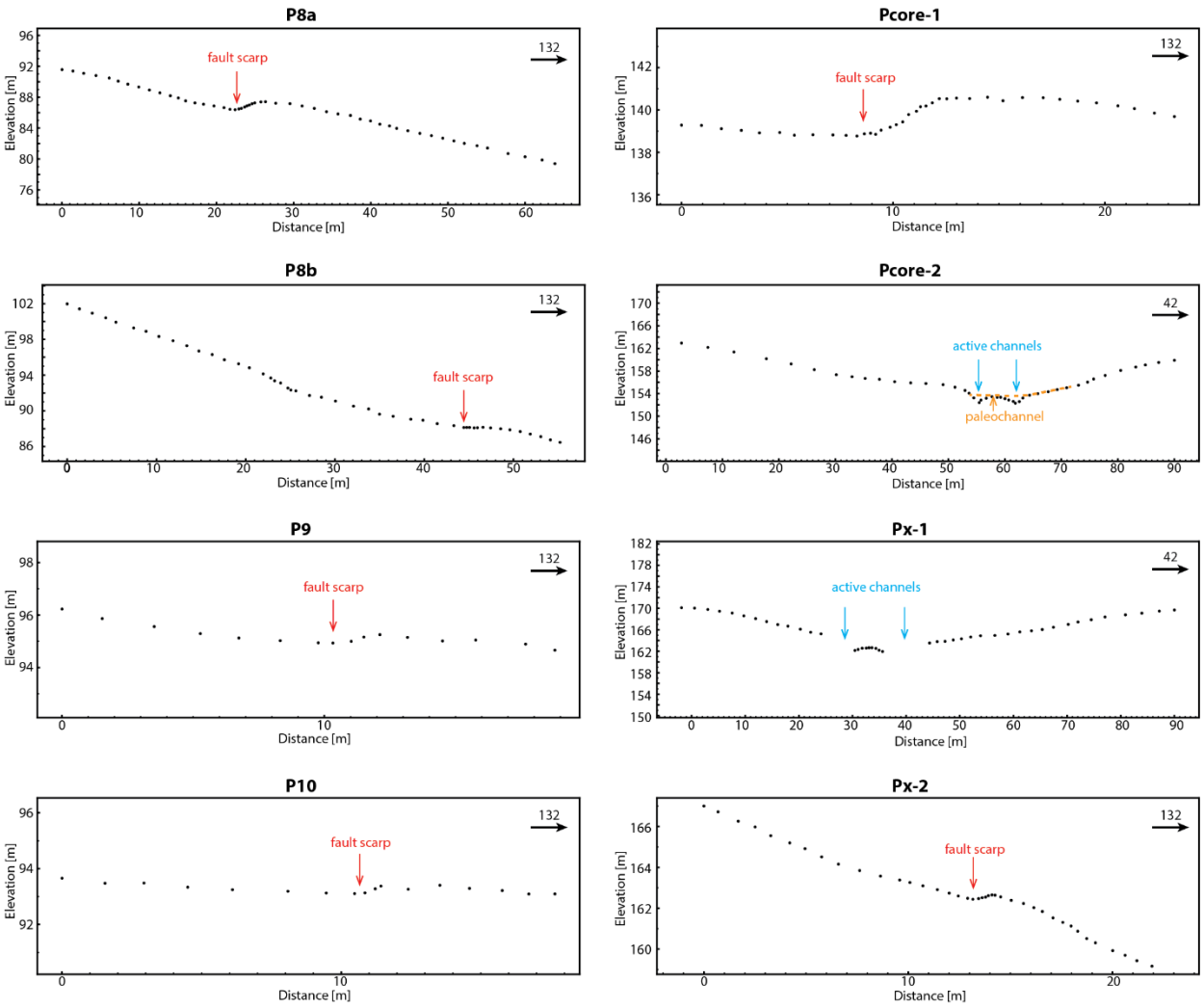

Fig. 7 Additional dGPS data profiles. Profile locations are shown in Figs. 2e and 4. Pcore-1 and Px-2 show the fault scarps of the offset paleochannel surfaces (Figs. 4 and 5). Pcroe-2 and Px-1 are generated by perpendicularly projecting the fault crest elevation data to a fault-parallel profile line.

Fig. 8 (next page) Images of sediment cores. The core locations are shown in Fig. 4b. Radiocarbon dating results and their calibrated ages are reported in Table 1. Relative vertical-direction locations of the core tops reflect the relative elevation changes of the ground surface. ST - strawberry color tephra

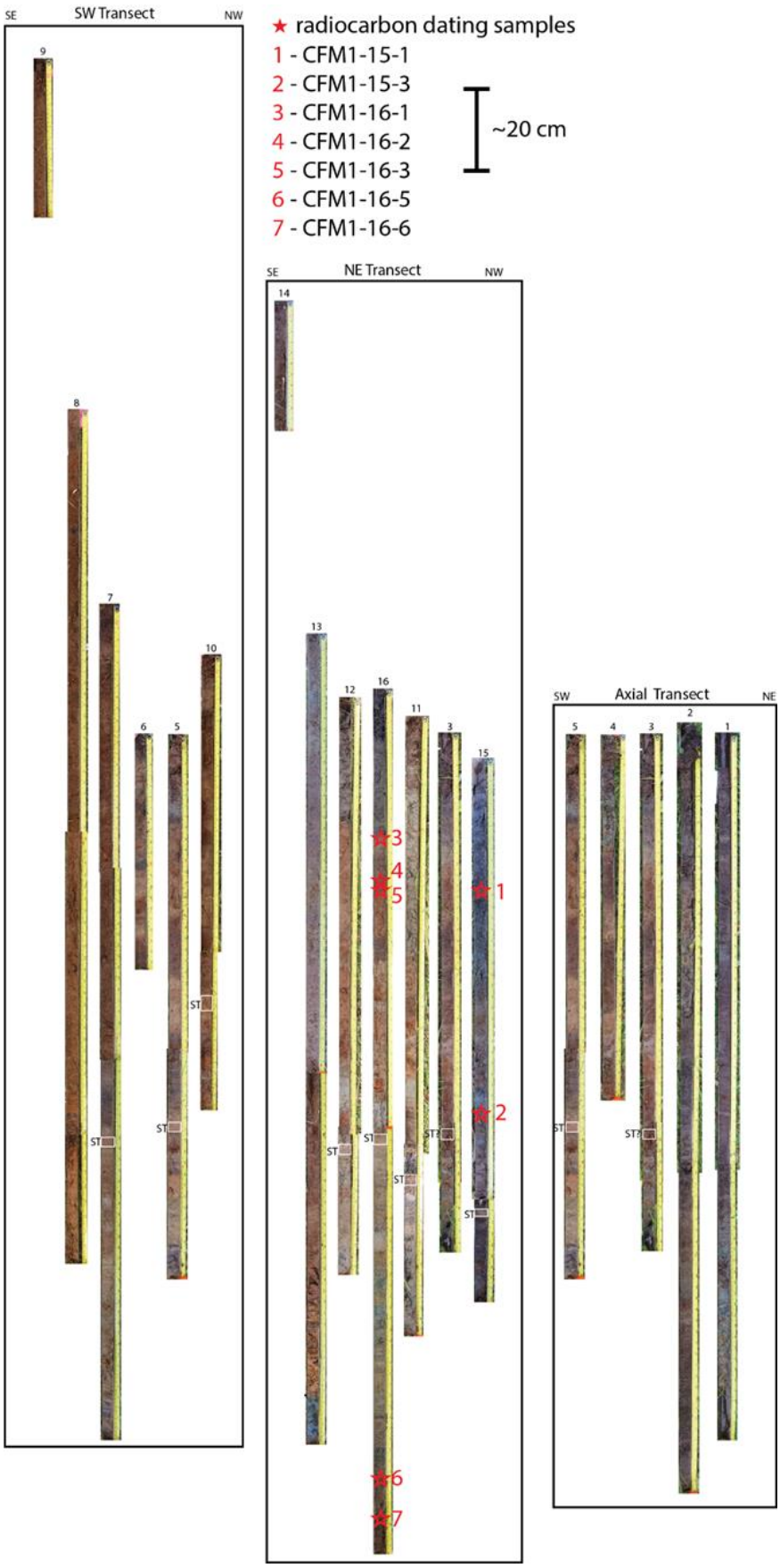
SE
SW Transect
NW
9
8
7
6
5
10
ST
ST
ST
★ radiocarbon dating samples
1 - CFM1-15-1
2 - CFM1-15-3
3 - CFM1-16-1
4 - CFM1-16-2
5 - CFM1-16-3
6 - CFM1-16-5
7 - CFM1-16-6
~20 cm
SE
NE Transect
NW
14
13
12
16
11
3
15
ST
ST
ST
ST
ST
ST
☆3
☆4
☆5
☆1
☆2
☆6
☆7
SW
Axial Transect
NE
5
4
3
2
1
ST
ST?

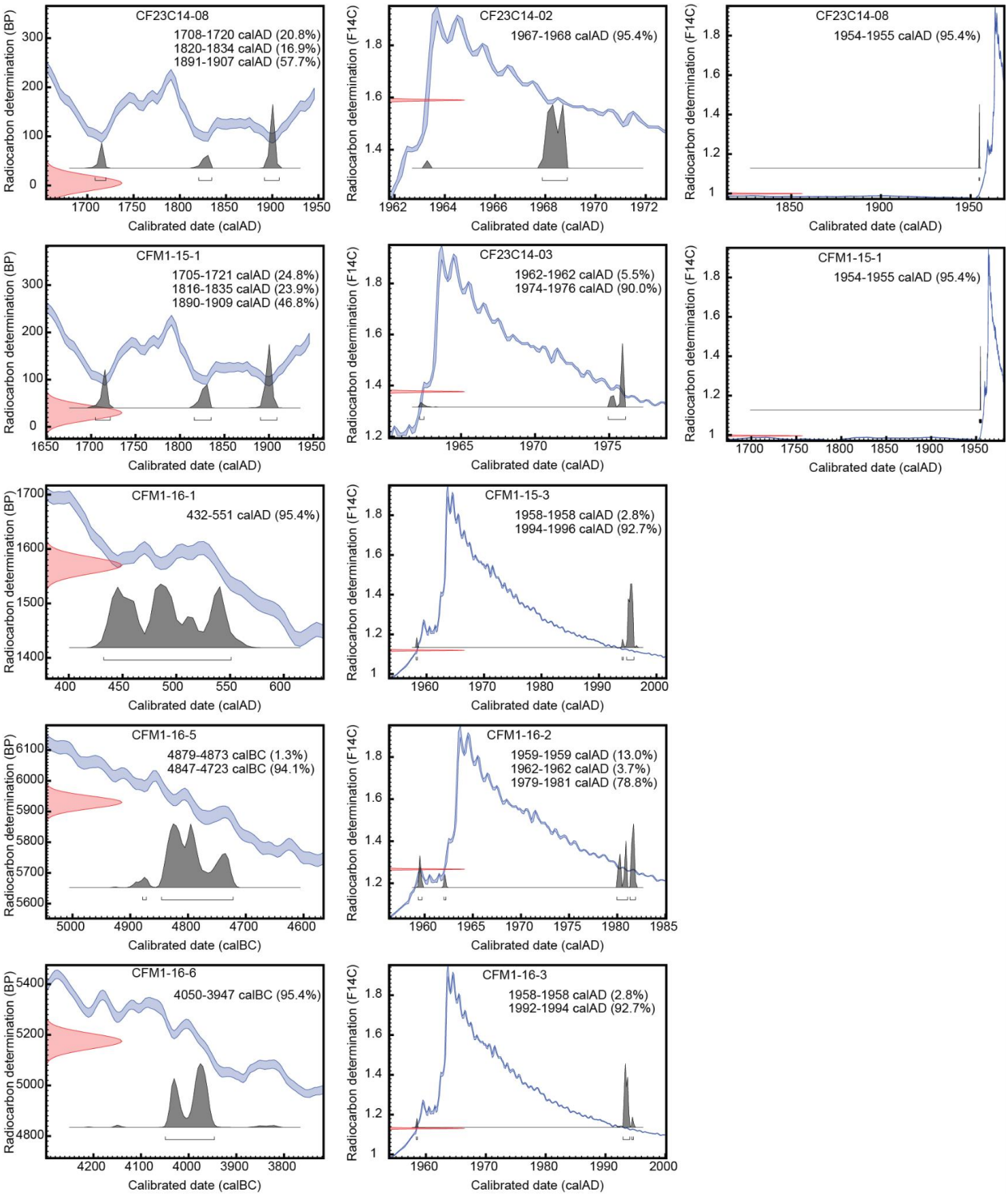

Fig. 9 Calibrations of radiocarbon dating results. The calibrations were conducted using OxCal (Ramsey, 2009) with the IntCal20 Northern Hemisphere Radiocarbon Age Calibration Curve (Reimer et al., 2020) and Bomb21NH1 curve (Hua et al., 2022). The raw ages of Samples CF23C14-08 and CFM1-15-1 are close to modern and this figure shows their calibration results using both curves.

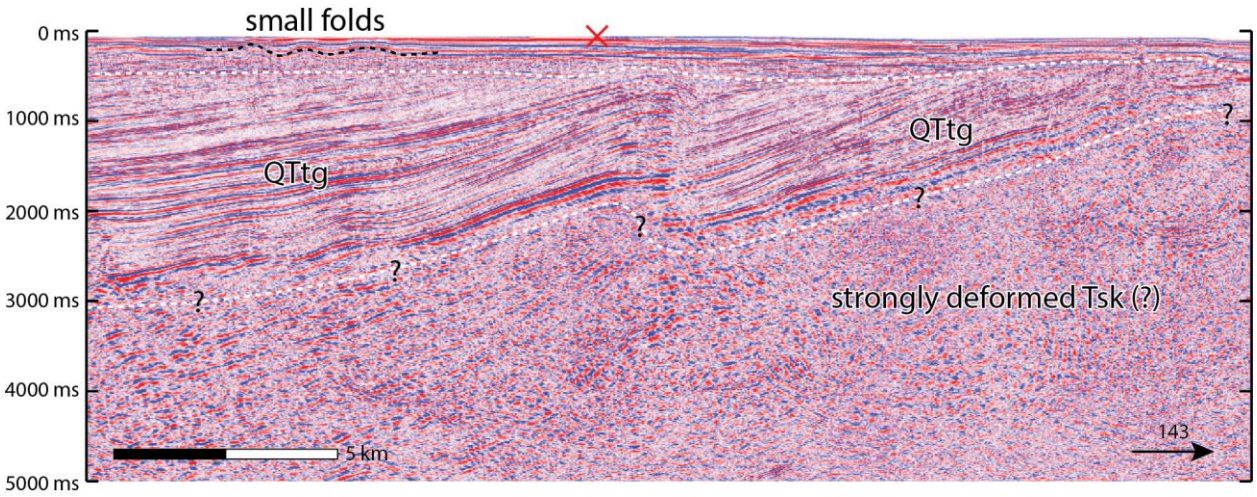

Fig. 10 Interpretation of a seismic image ~10 km northeast of Chirikof Island. The red cross shows the approximate location of the intersection between the along-strike projection of the fault and the transect. White dash lines are unconformities. QTtg – Tugidak Formation, Tsk – Sitkinak Formation

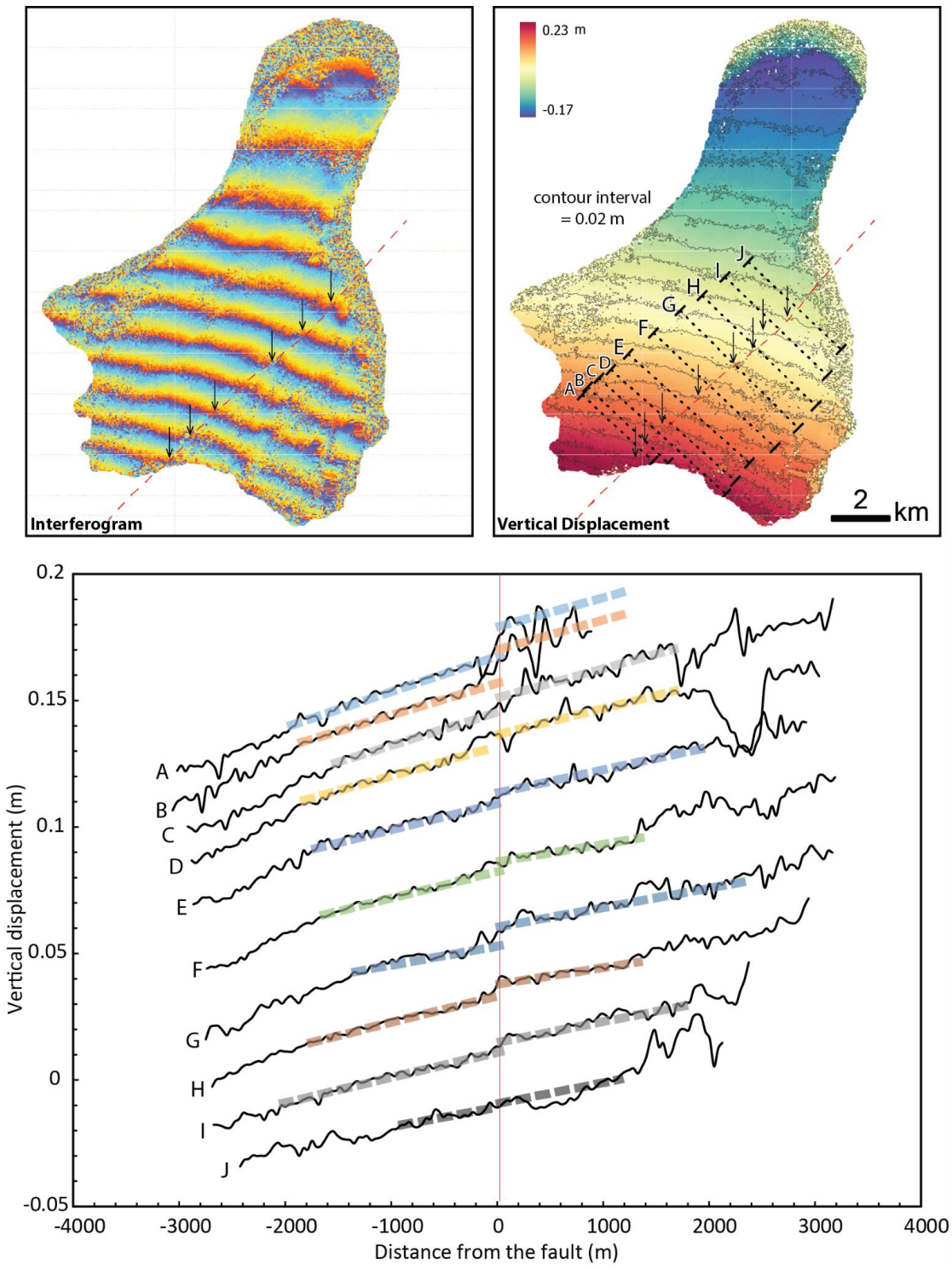

Fig. 11 InSAR interferogram, vertical displacement, vertical displacement profiles of Chirikof Island (07/19/2021-07/31/2021). The vertical displacement map is generated from the unwrapped differential phase measurements under the assumption that the displacement is entirely in the vertical direction. Positive values indicate uplift and negative values indicate subsidence.

Table 1. Radiocarbon dating results

Sample	Core/Pit	Depth (cm)	Fraction modern	±	δ14C (‰)	±	14C age (yr B.P.)	±	Calibrated age interval	prob %
CF23C14-02	OSL01	90	1.5900	0.0027	590.0	2.7	Modern		1967-1968 AD	95.4
CF23C14-03	OSL01	93-97	1.3763	0.0024	376.3	2.4	Modern		1974-1976 AD	90
CF23C14-08	OSL02	55-57	0.9991	0.0017	-0.9	1.7	5	15	1891-1907 AD	57.1
									1954-1955 AD	95.4
CFM1-15-1	CFM1-15	29-30	0.9966	0.0016	-3.4	1.6	30	15	1890-1909 AD	46.8
									1954-1955 AD	95.4
CFM1-15-3	CFM1-15	80-81	1.1195	0.0019	119.5	1.9	Modern		1994-1996 AD	92.7
CFM1-16-1	CFM1-16	34-36	0.8225	0.0014	-177.5	1.4	1570	15	432-551 AD	95.4
CFM1-16-2	CFM1-16	44-46	1.2670	0.0020	267.0	2.0	Modern		1979-1980 AD	78.8
CFM1-16-3	CFM1-16	46-47	1.1307	0.0020	130.7	2.0	Modern		1992-1994 AD	92.7
CFM1-16-5	CFM1-16	182-183	0.4781	0.0011	-521.9	1.1	5930	20	4847-4723 BC	94.1
CFM1-16-6	CFM1-16	191-193	0.5250	0.0017	-475.0	1.7	5175	30	4050-3947 BC	95.4

Ages were calibrated with Oxcal (Ramsey, 2009) using the IntCal20 Northern Hemisphere Radiocarbon Age Calibration Curve (Reimer et al., 2020) and Bomb21NH1 curve (Hua et al., 2022). The raw ages of Samples CF23C14-08 and CFM1-15-1 are close to modern and the table reports their calibration results using both curves. The calibrated age interval of the highest possibility is reported for each calibration in this table if more than one interval is yielded. Details of the calibrations are reported in Fig. 9.